

# Motion Detection Method for Clutter Rejection in the Bio-Radar Signal Processing

Carolina Gouveia, José Vieira, Pedro Pinho

**Abstract**—The cardiopulmonary signal monitoring, without the usage of contact electrodes or any type of in-body sensors, has several applications such as sleeping monitoring and continuous monitoring of vital signals in bedridden patients. This system has also applications in the vehicular environment to monitor the driver, in order to avoid any possible accident in case of cardiac failure. Thus, the bio-radar system proposed in this paper, can measure vital signals accurately by using the Doppler effect principle that relates the received signal properties with the distance change between the radar antennas and the person's chest-wall. Once the bio-radar aim is to monitor subjects in real-time and during long periods of time, it is impossible to guarantee the patient immobilization, hence their random motion will interfere in the acquired signals. In this paper, a mathematical model of the bio-radar is presented, as well as its simulation in MATLAB. The used algorithm for breath rate extraction is explained and a method for DC offsets removal based in a motion detection system is proposed. Furthermore, experimental tests were conducted with a view to prove that the unavoidable random motion can be used to estimate the DC offsets accurately and thus remove them successfully.

**Keywords**—Bio-signals, DC Component, Doppler Effect, ellipse fitting, radar, SDR.

## I. INTRODUCTION

THE sensorless measurement of bio-signals has the potential to improve many areas. In the medical field, among many other applications, it can be highlighted the continuous monitoring of vital signals in bedridden patients, as in a burn unit where physical contact with the patient is discouraged. Also for sleeping monitoring, namely to support cases of Obstructive Sleep Apnea Syndrome (OSA) without interfering in the normal life style of the patients, or in the prevention of Sudden Infant Death Syndrome (SIDS), [1]. In terms of commercial applications, it can be highlighted the driver monitor, where his vital signals are monitored to avoid any possible accident in case of cardiac failure. Applications in psychology are also possible, as for example measurement of stress response, [2].

The overall bio-radar's system is represented by the block diagram in Fig. 1. It is composed by a continuous wave Doppler radar which continuously transmits a sinusoidal carrier, generated digitally, and receives the echo from the reflecting target. Due to the Doppler effect, there is a phase change as the subject's chest-wall moves towards or away from

the radar and hence a phase modulation in the received signal is created [3].

The concept of non-contact signal extraction of human physiological parameters, has been demonstrated by pioneers during the 1970's, where both the respiration and heartbeat were measured separately during apnea interspersed periods, [4]-[6]. Later, between 1980's and 1990's this system was implemented using incorporated analog and digital signal processing. Thus, the state-of-the-art of these systems follows a time line of hardware implementation. The first proposed prototypes were implemented with transceivers composed by single Radio Frequency (RF) hardware components interconnected with each other, [7]. Later, the RF front-end components were integrated in a single chip using CMOS processes, [8]. Nowadays the research in this area is even more focused on the development of systems with features that guarantee low power, small dimensions, better accuracy, long range detection and more robust operation. With this in mind, in [9] a bio-radar implementation was proposed using a front-end based in Software Defined Radio (SDR) system. These radars allow the digital configuration of its input and outputs (receiver and transmitter), regarding the required frequency and sampling rate of the current application. These configurable systems present an advantage comparing with the previously referred ones, due to its flexibility and compact devices. In [9], signals were first acquired, recorded in binary files and then processed offline using MATLAB. Therefore, considering the work developed until the recent times, the bio-radar prototype developed for this work has a front-end based in SDR and operates in real-time, using the LabVIEW software for Digital Signal Processing (DSP) algorithm execution. In this way, the acquired signals can be processed and visualized during their acquisition time.

Bio-signals have low amplitude and the modulation that they create on the received signal will be, in the baseband, very close to DC. Hence they are highly sensitive to several sources of noise, such as clutter from the scenario reflections, which will increase the DC level in the acquired baseband signals. It will be seen further in this paper that the DC component interferes in the signal's recover and thus, it should be eliminated. In [3], [10] some techniques to remove DC are presented. However, as it will be described later in this work, this estimation depends in the arc projection, which can assume different shapes, turning difficult to estimate the arc centre accurately.

The applications of the bio-radar system encompass long term monitoring periods where it is impossible to guarantee the total immobilization of the patient. Once the phase modulation occurs due to the change of the distance travelled by the

C. Gouveia is with Instituto de Telecomunicações and Universidade de Aveiro, Aveiro, Portugal (e-mail: carolina.gouveia@ua.pt)

J. Vieira is with Instituto de Engenharia Electrónica e Telemática de Aveiro, Instituto de Telecomunicações and Universidade de Aveiro, Aveiro, Portugal (e-mail: jnvieira@ua.pt)

P. Pinho is with Instituto de Telecomunicações, Aveiro, Portugal and Instituto Superior de Engenharia de Lisboa, Portugal (e-mail: ppinho@deetc.isel.pt)

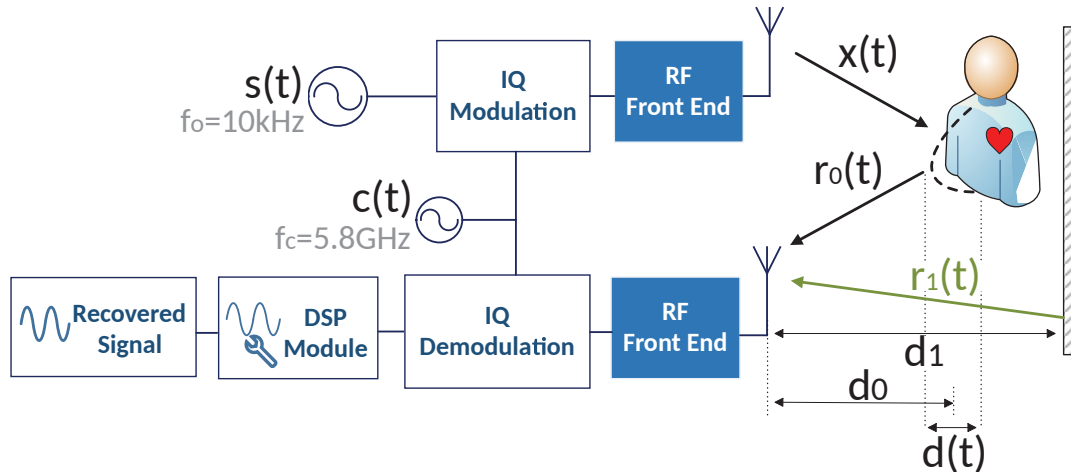


Fig. 1 Bio-Radar system block diagram

propagating wave, any motion of the subject, including the ones caused by other body parts, will cause phase modulation of the carrier that can mask the one caused by bio-signals. In [11], [12], some solutions for the random motion detection and cancellation are proposed.

In this paper a mathematical model that synthesises the bio-radar system behaviour is presented, considering a real scenario. In this framework, a simulation of the mathematical model is done, in order to study how the signal parameters influence the extracted signal, focusing in the DC component caused by clutter. Also an algorithm for the breathing signal extraction is presented, which includes a method for DC cancellation based on ellipse fitting. Regarding the challenges to find the best estimation of the DC offsets, a method is proposed which takes into account the random motion detected. Finally, experimental tests were conducted in order to understand how much the DC component changes with the displacement of the target and to prove that this method guarantees more accurate results in the DC estimation, if comparing with the results reported in [3] and [10].

This paper is organized as follows: the next section will start by presenting a mathematical model for the bio-radar system. Then the description of the breathing signal extraction algorithm is presented on Section II-B. Then, on Section III a simulation of the model is presented, in order to see the effect of DC in the extracted signal and thus understand the necessity of the method proposed in Section III-B. In Section IV, experimental tests are described. Finally, the results are discussed and the last section presents the conclusions. All the conducted tests were focused in the respiratory signal acquisition.

## II. MODELLING THE BIO-RADAR SYSTEM

### A. Signal Model for the Bio-Radar Channel Response

Regarding the block diagram presented in Fig. 1, a baseband signal is generated digitally, with a sampling rate  $f_s$ . The signal is a complex sinusoid with frequency  $\omega_0$ , and it is represented by (1).

$$s(n) = e^{j\omega_0 n} \quad (1)$$

Signal  $s(n)$  is then modulated with an in-phase and quadrature (IQ) modulation, with a carrier frequency  $\omega_c$ , leading to the signal of (2), that is transmitted towards the target.

$$x(t) = \cos[(\omega_0 + \omega_c)t] \quad (2)$$

The received signal, encompasses the time variant signal  $r_0(t)$  correspondent to the chest-wall reflection and the stationary signal  $r_1(t)$  which represents the sum of the total sources of clutter. The total signal on the receiver's input, can be expressed as in (3):

$$\begin{aligned} r(t) &= r_0(t) + r_1(t) = \\ &= A_0 \cos[(\omega_0 + \omega_c)t + \varphi(t)] + A_1 \cos[(\omega_0 + \omega_c)t + \theta_1] \end{aligned} \quad (3)$$

where  $A_0$  and  $A_1$  are the amplitudes of the received signal from the subject and clutter, respectively,  $\varphi(t)$  is the phase change function which contains the respiratory information and  $\theta_1$  is the phase change due to clutter. This phase change can be expressed as  $\theta_1 = 4\pi d_1/\lambda$ , considering that the clutter source is located at a distance  $d_1$  from the radar and  $\lambda$  is the wavelength. After its reception, signal  $r(t)$  is IQ demodulated resulting in (4), and it is sampled at the same sampling rate  $f_s$  used in the transmission channel.

$$g(n) = g_0(n) + g_1(n) = A_0 e^{j\varphi(n)} + A_1 e^{j\theta_1} \quad (4)$$

The phase change function  $\varphi(n)$ , results from the chest-wall motion, which changes the wave travelled distance and hence modulates the reflected signal. Thus, the phase change function can be described by (5):

$$\varphi(n) = \theta_0 + \frac{4\pi d(n)}{\lambda} \quad (5)$$

where  $\theta_0$ , is the phase corresponding to the average distance travelled by the wave, which can be expressed as  $\theta_0 = (4\pi d_o/\lambda) + \phi$ , considering the nominal distance between the radar and the target,  $d_o$ , and the phase shift at the target's surface,  $\phi$ . The respiratory component is described by  $4\pi d(n)/\lambda$  and in the remain of this work we consider the chest movement described as  $d(n) = a_r \cos(2\pi f_1 n)$ , where  $a_r$

is the amplitude of the chest movement and  $f_1$  is the breathing rate.

### B. Breathing Signal's Extraction Algorithm

The block diagram of Fig. 2 represents the receiver's channel. The received signal  $r(t)$  is sampled by the RF front-end and IQ demodulated, resulting in signal  $r_p(n)$ . This signal is then processed by the following DSP algorithm: the baseband complex signal  $g(n)$ , is downsampled once it is a low-pass signal. Fig. 3(a), represents the phase variation due to the target's motion, which consists in an arc in the complex diagram. In an ideal scenario without clutter, the arc fits to a perfect circle centred at zero. The length of the arc corresponds to the amplitude of the respiratory signal,  $a_r$ , which has a direct relation with the wavelength of the carrier signal. Higher carriers give more resolution, this means that regarding the same motion amplitude, lower wavelengths create larger arcs rather than higher wavelengths. The radius of the arc is the received signal's amplitude  $A_0$ . The arc position in circle varies with the distance between the radar and the target  $d_0$ .

In real-world scenarios there are some effects that change the obtained arc and could influence the accuracy in the breath rate extraction. For instance, the IQ imbalance effect occurs when both real and imaginary parts do not have the same amplitude and the phase relationship is not exactly  $90^\circ$ . Hence, the formed arc fits an ellipse instead of a circle. This paper will not focus in the imbalance compensation and its disturbance in the signal recover is neglected. However it will be considered that the arc fits an ellipse instead a circle.

There are also DC offsets present in both real and imaginary parts of the baseband signal  $g(n)$ , caused by the clutter, which leads to an offset of the arc's centre. The clutter signal,  $g_1(t)$  from (4), is the result of the sum of all multipath signals, as explained previously. The multipath effect in a real case scenario can be illustrated by a vectorial diagram, as in Fig. 3. The sum of all parasitic reflections  $r_a$ ,  $r_b$  and  $r_c$  results in a single vector,  $r_1$ .

The DC offsets are estimated and removed using the ellipse fitting method [13], which tracks the coordinates of the arc centre and subtract them from the complex signal, forcing the arc to be centred at zero.

After the DC compensation (signal  $b(n)$ ), a preliminary angle computation is done in order to evaluate if the arc is located between the  $2^{nd}$  and the  $3^{rd}$  quadrants of the complex diagram, once this location can cause wraps in the resulting signal. If so,  $b(n)$  is multiplied by an auxiliary complex signal  $aux(n)$ , which has the angle value required to change the arc position and thus avoid the wrap occurrence.

Finally, the arctangent is computed in order to extract the respiratory signal  $y(n)$ , which corresponds to (5), [1]-[3], and its rate is computed using the power spectral density.

## III. MOTION DETECTION BASED METHOD FOR DC CANCELLATION

### A. Model Simulation

The simulation started with the generation of the baseband signal, according to (4) and the assignment of the following

basic parameters: carrier frequency  $f_c = 5.8$  GHz, sampling frequency  $f_s = 100$  Hz, amplitude of the signal  $g(t)$  as  $A_0 = 0.1$ , initial phase shift as  $\phi = \pi/12$  rad and breathing frequency as  $f_1 = 0.3$  Hz.

Then, the signal from clutter was added and the arctangent was computed, regarding two different distances of the main target  $d_0$ , the clutter distance  $d_1 = 5$  m and the amplitude of the clutter signal  $A_1 = 0.5$ . Fig. 4 shows the arc obtained for each simulation and the extracted signal, respectively.

Regarding Fig. 4, it is possible to conclude that for an accurate arctangent result, the formed arc should be centred in the origin of the complex axis. If the arc's centre is shifted, as shown in Figs. 4(a) and 4(c), the arc will be projected wrongly in the axis, resulting in signal distortion and also the amplitude of the extracted signal will decrease deeply. This signal distortion will severely interfere in the breath rate computation, specially in cases such Fig. 4(b), where a second wave appears.

### B. Method Proposal

In Section II-B, an algorithm for the respiratory signal extraction is presented, where the ellipse fitting method is used to remove the DC offsets. As previously mentioned, the ellipse fitting method estimates the coordinates of the arc's centre. Arcs from real acquisitions do not have a perfect shape due to the IQ imbalance and the irregularity in the breathing amplitude will lead to a dispersion of the arc drawing, instead of a thin line. Thus, this estimation is a challenging task and therefore a new method is proposed in order to improve this estimation. It consists in the usage of the full ellipse information rather than the arc, and thus more samples uniformly distributed are considered, resulting in a more accurate estimation of the arc's centre. This new method can be summarized by the block diagram in Fig. 2 and from now on it is going to be referred as the Full Ellipse Method with Detectable Motion (FEMDM). In this framework, for comparison purposes, the conventional arc method it is going to be referred as the Arc Method (AM).

The full ellipse information can be obtained when the target displacement is superior to the wavelength. Considering real scenarios of long term monitoring periods, as in vehicular applications, it is impossible to avoid random motions of the subjects. These random motions are detected by the radar, together with the respiratory signal and they stand out once their amplitude is higher than the amplitude from vital signals (usually above the wavelength). Thus, everytime a random motion is detected, the breathing rate measurement can be suspended and the ellipse fitting can be computed. The arc's centre coordinates are updated and thus the DC offsets are eliminated periodically. Once without DC, the signal can be decimated and the arctangent computed afterwards.

This algorithm should be performed in real time, so its efficiency depends if the DC value do not vary significantly with the target displacement, otherwise more time is required for its update.

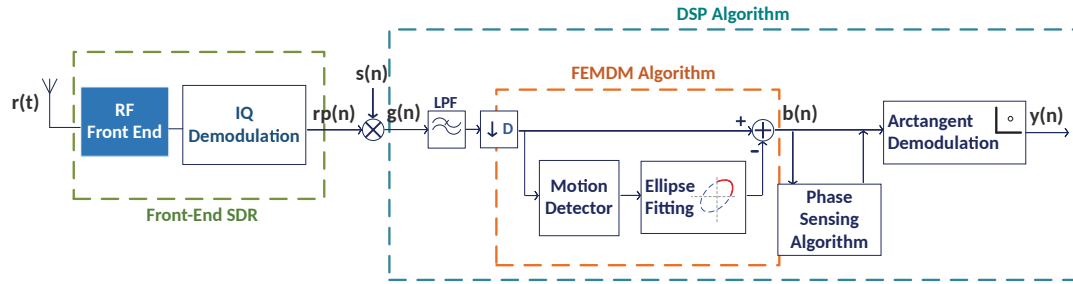


Fig. 2 Receiver channel with DSP algorithm implementation

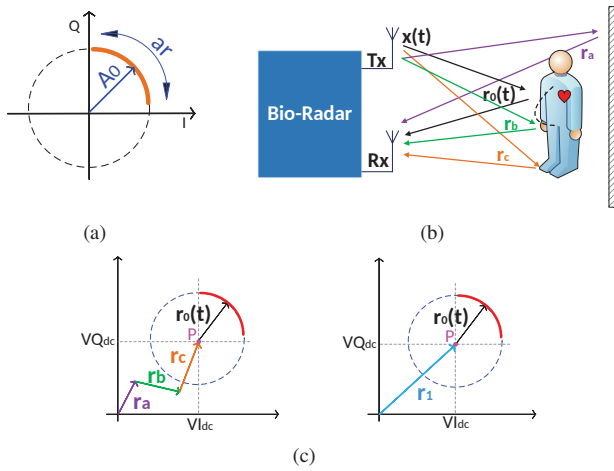


Fig. 3 Effect of clutter: (a) Complex plot of the baseband signal  $g(n)$  due to the target motion, (b) Representation of the parasitic reflections in a real scenario, (c) Vectorial diagram of the received signal considering clutter

#### IV. IMPLEMENTATION

Experimental tests were performed using the bio-radar setup, shown in Fig. 5(a).

The bio-radar prototype consists in a real-time measurement system, implemented in the LabVIEW software. Signals are acquired using two antennas, one for transmission and the other for reception, which works with a carrier frequency equal to 5.8 GHz, and the front-end based in a SDR system, which is a reconfigurable platform that establishes the connection of the front-end hardware and the DSP software, as explained previously. In the framework of this application, the SDR used is an USRP B210.

The results from Section V were obtained using MATLAB. In order to accomplish the ellipse fitting, an *Ellipse Fitting Function* based in the least square fitting method was implemented. This function finds the best fit to an ellipse for a given set of points [14], and is also capable to determine the coordinates of its centre and thus estimate the DC component.

The conducted experiments used the Chest-Wall Simulator (CWS) (Fig. 5(b)) to simulate the chest-wall motion due to respiration, which moves with a frequency equal to 0.4 Hz. Thus, the same acquisition conditions are guaranteed once its motion keeps the same amplitude and frequency over time.

The practical procedure consisted in a signal acquisition, where the CWS motion was recorded for 15 seconds and then its position is manually changed several times by 5 cm.

This procedure was done twice and both extracted signals are shown in Fig. 6, and will be called as signal 1 ( $s_1(t)$ ) and signal 2 ( $s_2(t)$ ), respectively. They present two different behaviours intercalated: one sinusoidal signal, as result of the normal CWS motion and a high frequency signal with higher amplitude that results from the CWS displacement over its current position. These high frequency signals will be used estimate accurately the DC offsets.

For each acquisition, each signal was divided in several slots as shown in Fig. 6. Therefore, slots A-G correspond to the CWS motion and M1-M6 correspond to the CWS position change. Later on, the DC offsets were estimated by computing the length of vector  $r_1$  from Fig. 3(c). To evaluate and compare the DC value obtained by the FEMDM and AM, the absolute value from the coordinates of the centre (marked as the point P) was computed. Results and their discussion are presented in the next section.

#### V. RESULTS DISCUSSION

Attempting the experimental procedure described in the previous section, Fig. 6 shows the result of the arctangent computation of both acquired signals,  $s_1(t)$  and  $s_2(t)$ , prior to the DSP implementation.

Before the results discussion, an important detail of these signals should be pointed out. Regarding Fig. 6(a) from  $s_1(t)$ , there is a signal distortion due to an inaccurate computation of the arctangent. This distortion occurs due to the DC presence and results in different waveforms, for example, in slots B and C a second peak is present with smaller amplitude, in slots E and F the sinusoidal waveform is changed and finally all slots A to G have different amplitudes (slot D has its amplitude severely decreased). The same forms of distortion can be observed in Fig. 6(b) from  $s_2(t)$ , namely the small amplitude in slots D and E and the waveform change in slots E and F.

Back to the results discussion and beginning with  $s_1(t)$ , in Table I is presented the DC offsets estimation, obtained by both FEMDM and AM. In particular, the P point corresponds to the centre estimation and is represented by the complex number  $P = VI_{dc} + j * VQ_{dc}$ , where  $VI_{dc}$  and  $VQ_{dc}$  are the DC offsets and the  $|r_1|$  is the absolute value of the P point.

The results shown in Table I(a) correspond to the length of vector  $r_1$  using each arc from slots A-G and the ones present in Table I(b) correspond to the same results but using the M slots instead.

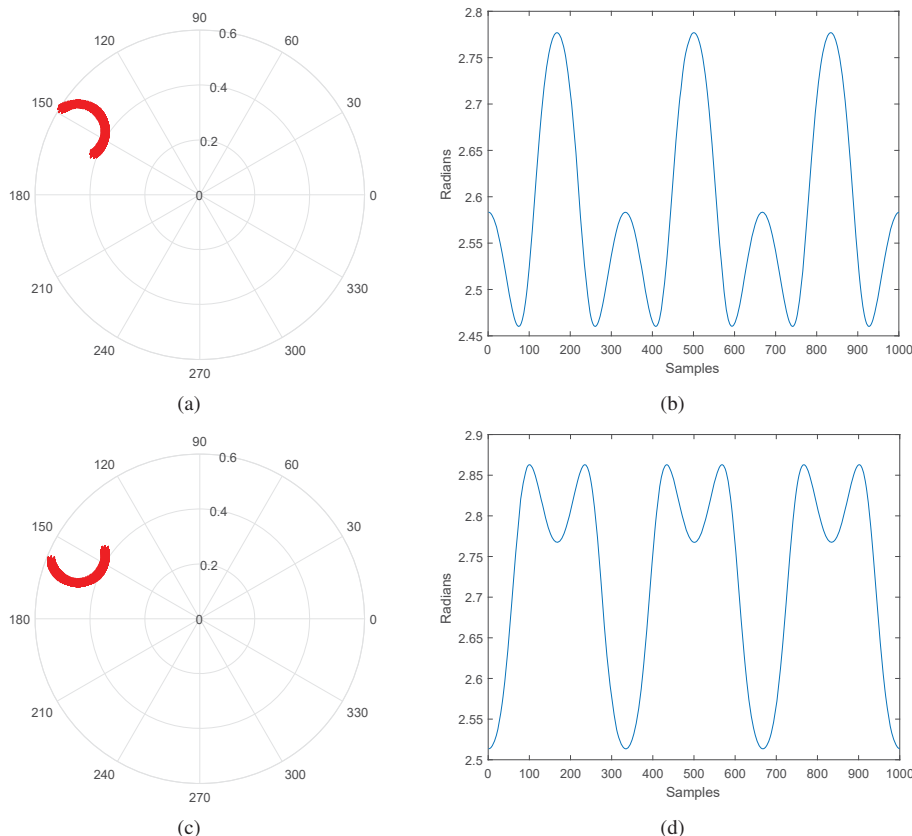


Fig. 4 Arc in the complex plot and respective extracted signal: (a), (b) for  $d_0 = 3$  m and (c), (d) for  $d_0 = 4$  m

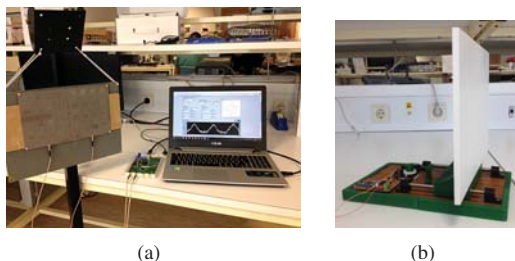


Fig. 5 Experimental set-up: (a) Bio-radar prototype, (b) Chest-wall simulator

TABLE I  
ARC CENTRE ESTIMATION USING CWS -  $s_1(t)$

(a) Using AM*			(b) Using FEMDM*		
	$P$	$ r_1 $		$P$	$ r_1 $
<b>A</b>	$-2.3 - 6.4i$	6.9	<b>M1</b>	$0.0 - 6.3i$	6.3
<b>B</b>	$2.0 - 9.3i$	9.5	<b>M2</b>	$-0.3 - 6.2i$	6.2
<b>C</b>	$5.7 - 28.4i$	28.9	<b>M3</b>	$-0.4 - 6.4i$	6.4
<b>D</b>	$4.1 - 3.9i$	5.7	<b>M4</b>	$-0.3 - 6.6i$	6.6
<b>E</b>	$1.6 - 3.3i$	3.7	<b>M5</b>	$0.2 - 6.5i$	6.5
<b>F</b>	$0.8 - 2.7i$	2.8	<b>M6</b>	$-0.2 - 6.1i$	6.1
<b>G</b>	$0.1 - 9.0i$	9.0			

\*all the results are multiplied by  $(\times 10^{-3})$

Concerning these results, some conclusions can be made. First, from the result of  $|r_1|$  from both methods, it is possible to conclude that the DC component does not change significantly when the target moves or change its position. Thus, it is

possible to apply the method proposed in this paper by updating the arc coordinates when an unexpected motion occurs and removing the DC offset afterwards, during the monitoring period. Moreover, despite the results correspondent to AM do not variate largely, the ones obtained from the FEMDM are more stable around the same value, which proves that the full ellipse should be used to estimate the DC component, as it gives more accurate results.

The optimal performance of this method can be observed in Figs. 7 and 8. Fig. 7 is an example of this method operation principal: Figs. 7 (a)-(c) represent the AM implementation using slot A, slot C and slot E respectively. It can be noticed that each arc has a different format, which leads to different DC offsets estimations. In contrast, Fig. 7(d) shows the exploitation of motion to do the ellipse fitting. For all slots M, the centre remains approximately the same.

Fig. 8 shows the vectorial diagram of the complex signal, with and without DC, using both methods AM and FEMDM for comparison purposes. Thus, Fig. 8(a) shows the complex signal with DC, where  $r_1$  is the DC vector which should be decreased after the AM or FEMDM application. The vector  $r_0(t)$  corresponds to the motion information that needs to be extracted along with the arc, with the DSP algorithm previously described. Figs. 8(b) and 8(c) show the complex signal after the methods application and it can be pointed out that both recentre the arcs back to the origin. In the case of FEMDM, the arcs are uniformly distributed around the origin,

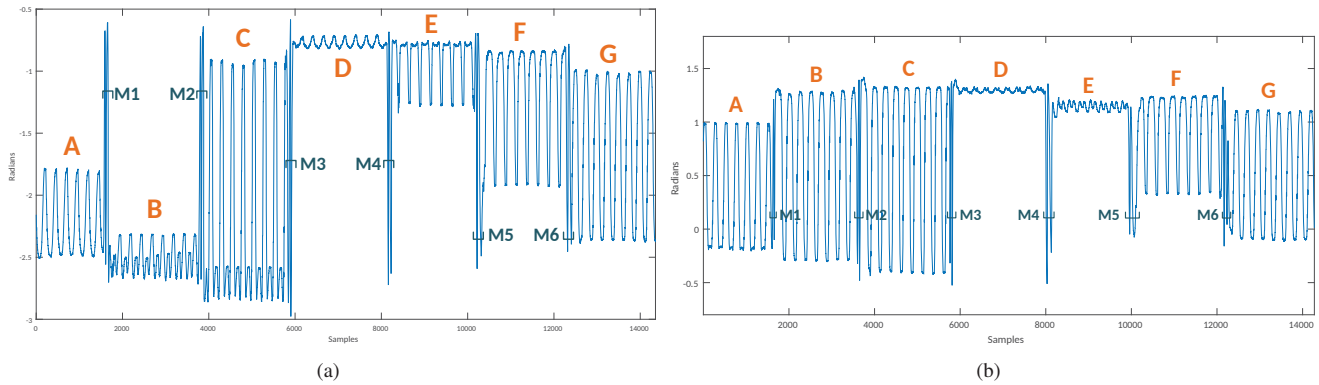


Fig. 6 Extracted CWS motion from the arctangent: (a)  $s_1(t)$ , (b)  $s_2(t)$

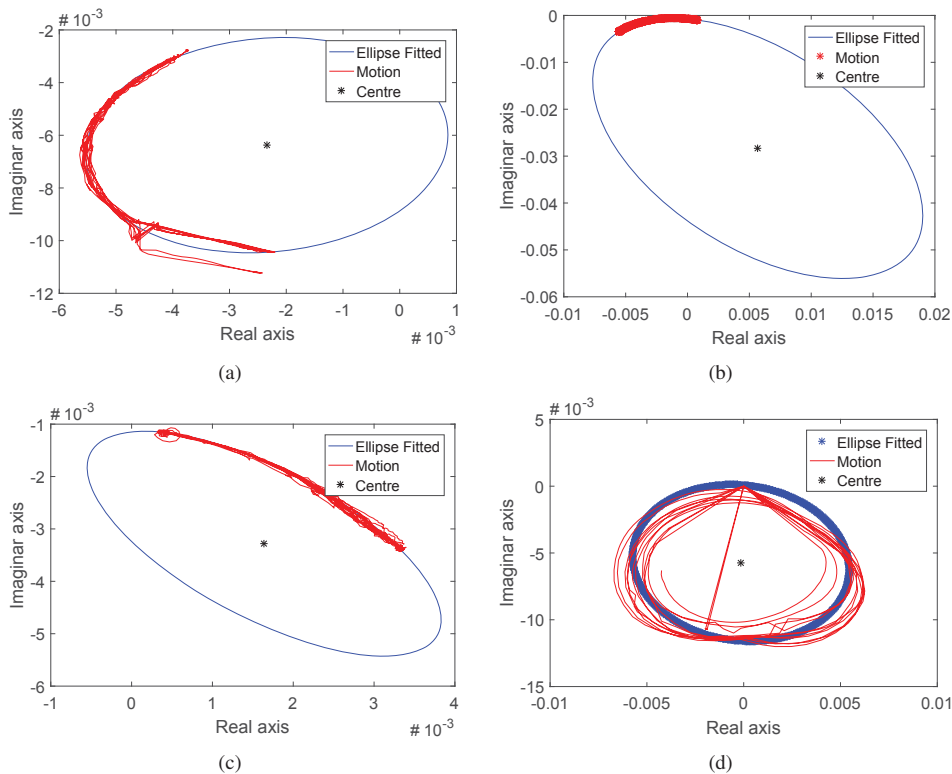


Fig. 7 Ellipse fitting using AM and FEMDM: (a) AM for slot A (b) AM for slot C, (c) AM for slot E, (d) FEMDM for the concatenation of all slots M1-M6

hence the  $r_0(t)$  length is approximately the same for all slots. On the other hand, the AM presents different  $r_0(t)$  lengths for the different slots of the same signal, which proves that this method can not guarantee the accuracy of the DC removal. Therefore, the extracted signal can be affected. Fig. 9 shows the extracted signals after the FEMDM and AM application and the arctangent computation. In Fig. 9(a), where the AM was used, amplitudes from slots B, C and G are smaller once their correspondent arcs are too far away from the origin. On the other hand, all the slots from Fig. 9(b) have the same amplitude approximately and there is no distortion in slots B, C, D and E due to the optimal efficiency of FEMDM method.

Regarding now the results obtained for  $s_2(t)$ , the Table II shows the values of DC offsets for both methods AM and FEMDM, and the same conclusions can be made: with AM

the value of  $|r_1|$  varies largely between slots, when compared with the one achieved with the FEMDM method.

TABLE II  
 ARC CENTRE ESTIMATION USING CWS -  $s_2(t)$

	(a) using AM*		(b) using FEMDM*	
	$P$	$ r_1 $	$P$	$ r_1 $
<b>A</b>	$5.6 + 3.6i$	6.6	<b>M1</b>	$4.8 + 3.2i$ 5.8
<b>B</b>	$6.7 + 3.9i$	7.8	<b>M2</b>	$5.4 + 3.4i$ 6.4
<b>C</b>	$6.0 + 3.2i$	6.8	<b>M3</b>	$5.6 + 3.5i$ 6.6
<b>D</b>	$3.8 + 1.2i$	4.0	<b>M4</b>	$5.2 + 3.3i$ 6.1
<b>E</b>	$2.5 - 4.0i$	4.8	<b>M5</b>	$5.0 + 3.2i$ 5.9
<b>F</b>	$1.9 + 2.4i$	3.1	<b>M6</b>	$4.8 + 3.2i$ 5.7
<b>G</b>	$3.0 + 1.5i$	3.4		

\*all the results are multiplied by  $(\times 10^{-3})$

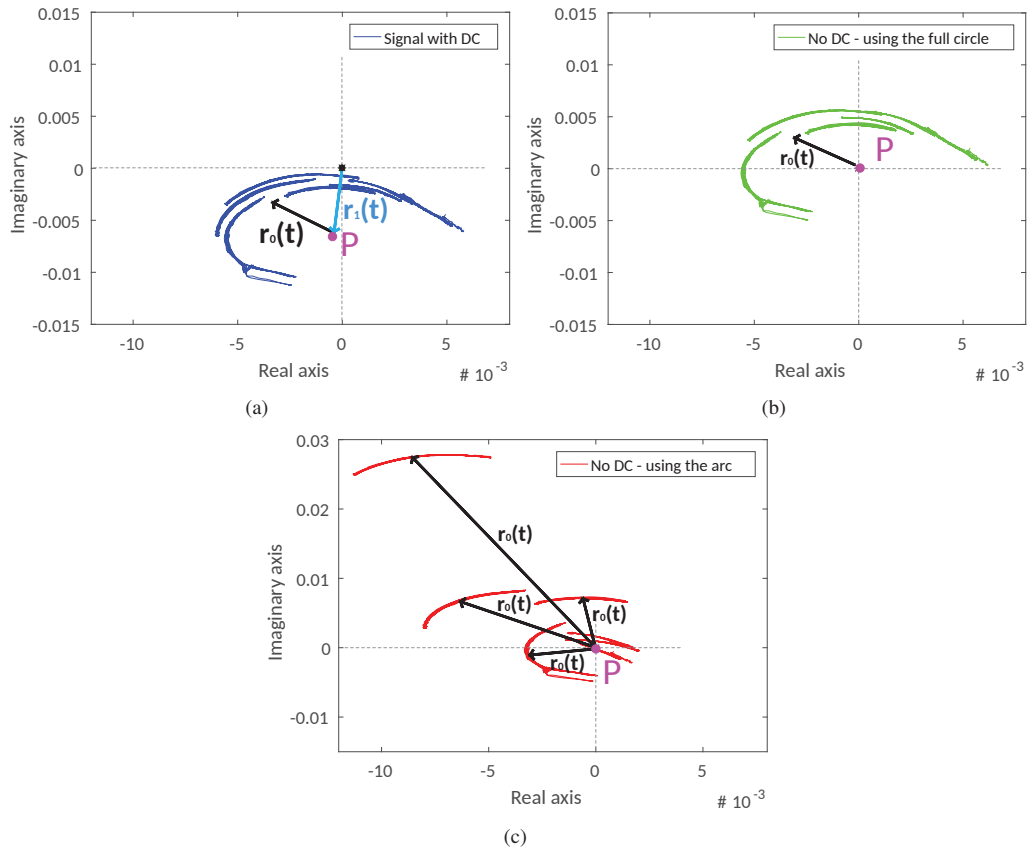


Fig. 8 Performance evaluation of FEMDM regarding the vectorial diagram of  $s_1(t)$ : (a) Original signal with DC component (b) Signal after DC removal using FEMDM, (c) Signal after DC removal using AM

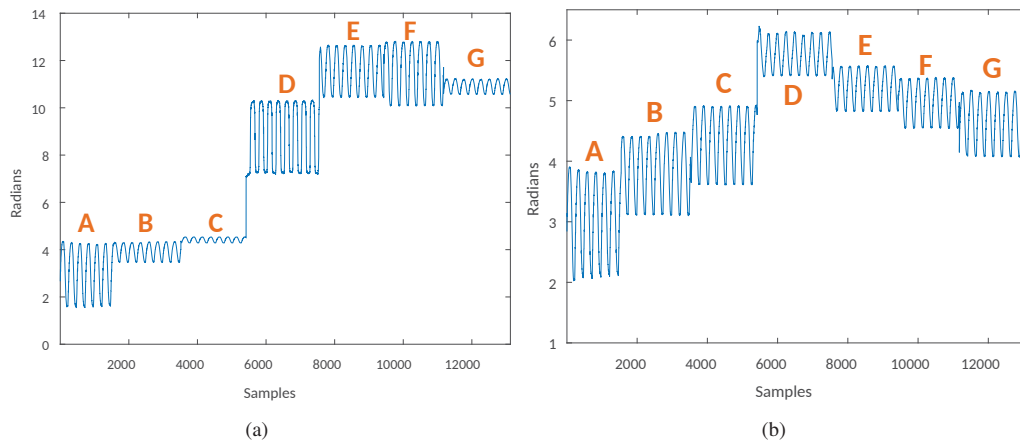


Fig. 9 Final angle computation of  $s_1(t)$  for both methods: (a) AM, (b) FEMDM

The complex plots and the vectorial diagram were also analysed and they are present in Fig. 10. After the arcs centre back to the origin, as shown in Figs. 10 (a) and (b), it is possible to visualize that using AM, the arcs are badly distributed as in the case of  $s_1(t)$ , hence this leads to the difference in the amplitudes in the extracted signal from Fig. 11(a), differently from the FEMDM case, which shows once more its efficiency.

## VI. CONCLUSION

In this work a mathematical model of the bio-radar system was introduced, as well as the DSP algorithm needed for phase demodulation and respiratory signal extraction. A simulation of the mathematical model is performed in order to evaluate the influence of clutter in the extracted signal. Focusing in the accuracy of the DC removal, some experimental tests were conducted to measure if the DC component changes with the target motion and to compare the performance of the

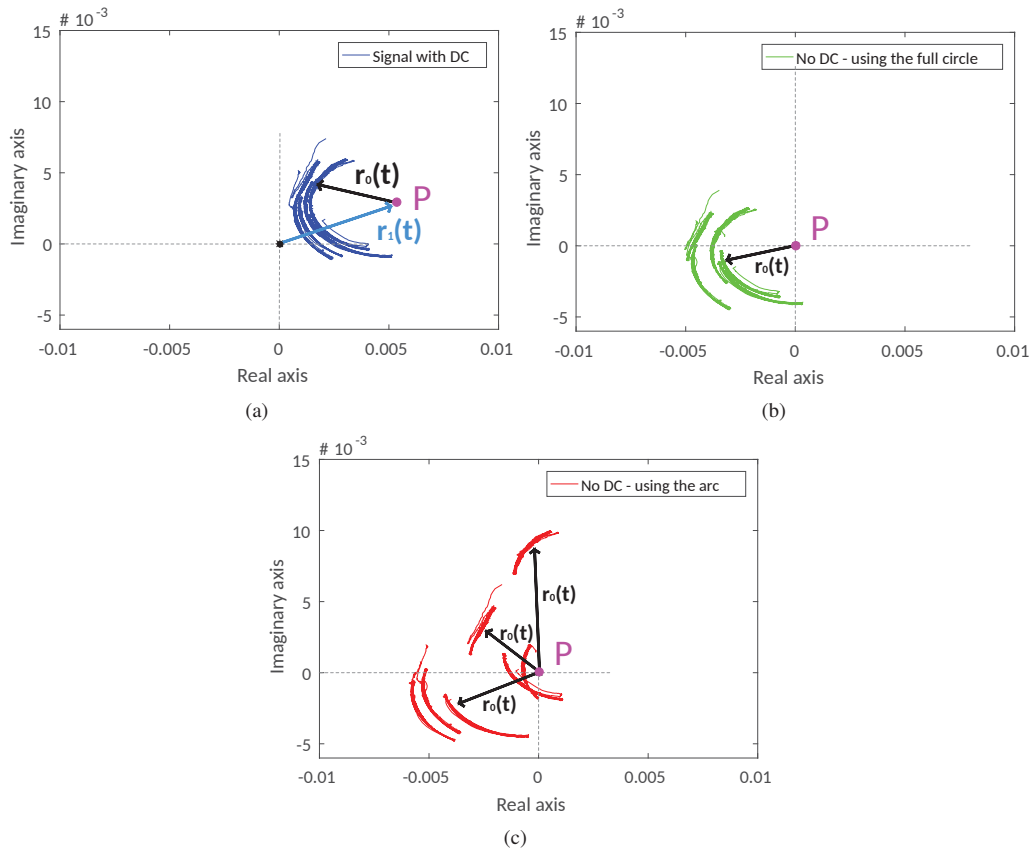


Fig. 10 Performance evaluation of FEMDM regarding the vectorial diagram of  $s_2(t)$ : (a) Original signal with DC component (b) Signal after DC removal using FEMDM, (c) Signal after DC removal using AM

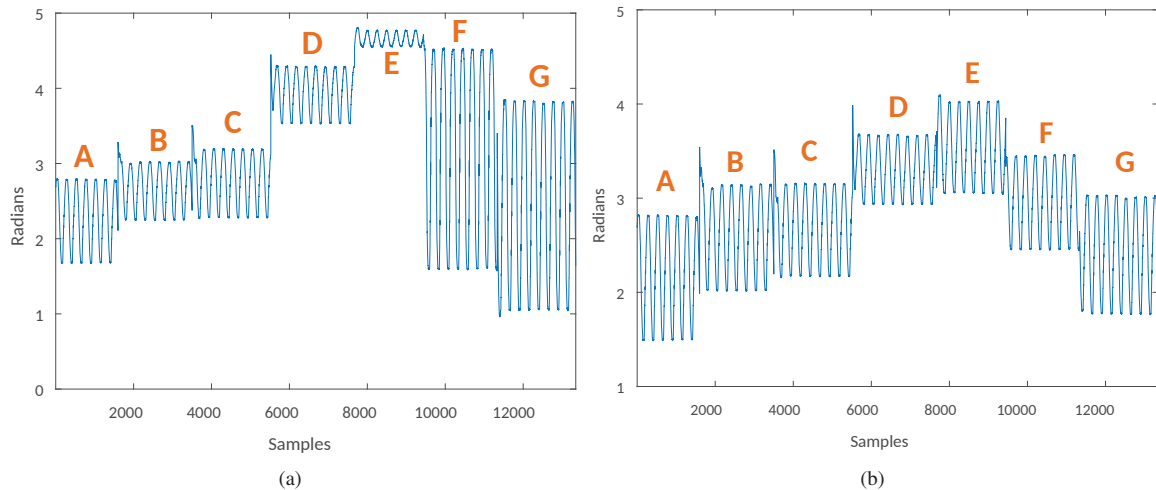


Fig. 11 Final angle computation of  $s_2(t)$  for both methods: (a) AM, (b) FEMDM

DC offsets cancellation using the AM and FEMDM methods. Results show that the DC component does not change abruptly, so it is possible to update continuously the value of DC offsets and remove it in real-time. It was also possible to conclude that the usage of full ellipse gives more accurate results for the DC offsets estimation, hence their removal can be more efficient under these conditions. As future work, it is intended to develop an algorithm for motion detection in real-time, in

order to complete the new DSP algorithm proposed in this paper.

#### ACKNOWLEDGMENT

This work is supported by the European Regional Development Fund (FEDER), through the Competitiveness and Internationalization Operational Programme (COMPETE



2020) of the Portugal 2020 framework [Project TexBoost with Nr. 024523 (POCI-01-0247-FEDER-024523)].

#### REFERENCES

- [1] C. Li, V. Lubecke, O. Boric-Lubecke, and J. Lin, "A Review on Recent Advances in Doppler Radar Sensors for Noncontact Healthcare Monitoring," *IEEE Transactions on Microwave Theory and Techniques*, **61**, 5, 2013, pp. 2046-2060.
- [2] D. Malafaia, et. al., "Cognitive Bio-Radar: The Natural Evolution of Bio-Signals Measurement," *Journal of Medical Systems*, **40**, 10, 2016, p. 219.
- [3] O. Boric-Lubecke, V. Lubecke, A. Droitcour, B. Park, and A. Singh, *Doppler Radar Physiological Sensing*, John Wiley & Sons, 2015.
- [4] J. C. Lin, Non-Invasive Microwave Measurement of Respiration, *Proceedings of the IEEE*, **63**, 10, 1975, p. 1530.
- [5] J. C. Lin, E. Dawe and J. Majcherek, A Non-Invasive Microwave Apnea Detector, *Proceedings of the San Diego Biomedical Symposium*, **16**, 1977, p. 441.
- [6] J. C. Lin, J. Kiernicki, M. Kiernicki and P. B. Wollschlaeger, Microwave Apexcardiography, *IEEE Transactions on Microwave Theory and Techniques*, **27**, 6, 1979, pp. 618-620.
- [7] K. H. Chan, J. C. Lin, *Microprocessor-based Cardiopulmonary Rate Monitor*, Medical and Biological Engineering and Computing, Springer, **25**, 1, 1987, pp. 41-44.
- [8] C. Li, X. Yu, C. M. Lee, D. Li, L. Ran, and J. Lin, "High Sensitivity Software Configurable 5.8 GHz Radar Sensor Receiver Chip in 0.13  $\mu\text{m}$  CMOS for Non-Contact Vital Sign Detection," *IEEE Transactions on Microwave Theory and Techniques*, **58**, 5, 2010, pp. 1410-1419.
- [9] D. Malafaia, J. Vieira and A. Tomé, "Improving Performance of Bio-Radars for Remote Heartbeat and Breathing Detection by using Cyclostationary Features," *Proceedings of the International Joint Conference on Biomedical Engineering Systems and Technologies*, **4**, pp. 344-349.
- [10] M. Zakrzewski, H. Raitinen, and J. Vanhala, "Comparison of Center Estimation Algorithms for Heart and Respiration Monitoring with Microwave Doppler Radar," *IEEE Sensors Journal*, **12**, 3, 2012, pp. 627-634.
- [11] Q.Lv, Y. Dong, Y. Sun, C. Li and L. Ran, "Detection of bio-signals from body movement based on high-dynamic-range Doppler radar sensor", RF and Wireless Technologies for Biomedical and Healthcare Applications (IMWS-BIO), 2015 IEEE MTT-S, 2015 International Microwave Workshop Series, 2015, pp. 88-89.
- [12] A. Vergara, N. Petrochilos, O. Boric-Lubecke, A. Host-Madsen and V. Lubecke, "Blind source separation of human body motion using direct conversion Doppler radar", *Microwave Symposium Digest*, 2008 IEEE MTT-S International, 2008, pp. 1321-1324.
- [13] B. Park, V. Lubecke, O. Boric-Lubecke, and A. Høst-Madsen, "Center Tracking Quadrature Demodulation for a Doppler Radar Motion Detector," *Microwave Symposium IEEE/MTT-S International*, 2007, pp. 1323-1326.
- [14] O. Gal, "Ellipse Fit using Least Squares criterion", <http://it.mathworks.com/matlabcentral/fileexchange/3215-fit-ellipse>, accessed: 2018